Article:

Zhu, L, Zhu, D, Sheng, Y et al. (2022) Polydopamine-coated magnetic montmorillonite immobilized with potassium copper hexacyanoferrate for selective removal of Cs+ and its facile recovery. Applied Clay Science, 216. 106367. ISSN: 0169-1317

https://doi.org/10.1016/j.clay.2021.106367

Polydopamine-coated magnetic montmorillonite immobilized with potassium copper hexacyanoferrate for selective removal of Cs^+ and its facile recovery

Lingdan Zhu[a], Deqin Zhu[a], Yu Sheng[a], Jiajia Xu[a], David Harbottle[b], Huagui Zhang[a,*]

[a]*College of Chemistry and Materials Science, Fujian Key Laboratory of Polymer Science, Fujian Provincial Key Laboratory of Advanced Materials Oriented Chemical Engineering, Fujian Normal University, Fuzhou 350007, China*

[b]*School of Chemical and Process Engineering, University of Leeds, Leeds LS2 9JT, UK*

Abstract

To address the challenges in remediating cesium contaminated aqueous environments, a low-cost, magnetically recoverable and superior composite adsorbent was fabricated based on the concept of magnetizing montmorillonite and entrapping potassium copper hexacyanoferrate that offers excellent selectivity for Cs^+. The facile, green and scalable synthesis route involved exchanging the interlayer ions of montmorillonite with ferrous ions before oxidizing to form magnetic montmorillonite using a low-temperature hydrothermal method. The composite was then coated with polydopamine to be complexed with copper ions and subsequently reacted with the hexacyanoferrate precursor to *in situ* grow potassium copper hexacyanoferrate nanoparticles, thus forming the composite, D-Mt-Mag-HCF. The adsorbent exhibited excellent Cs^+ sorption capacity (~159.2 mg/g) and Cs^+ selectivity greater than 8.2×10^4 mL g^{-1} in concentrated brine. Moreover, the magnetic properties (17.4 emu/g) of the adsorbent facilitated its separation from contaminated aqueous environments once the adsorbent had removed Cs^+. The current study demonstrates a novel and scalable production of a composite adsorbent that can be readily used to remediate contaminated water.

Keywords

Cesium removal; Magnetically recoverable adsorbent; Montmorillonite; Hexacyanoferrate; Polydopamine

1. Introduction

Nuclear power has demonstrated its great advantages in energy sector with its low unit cost, low pollution and its high efficiency in solving resource shortages and reducing carbon emissions (Kim et al., 2017a). Meanwhile, the drawback of the nuclear industry is also conspicuous as witnessed by the two well-known nuclear accidents at Chernobyl and Fukushima (Ding et al., 2016), that is, the disastrous radioactive contamination and spreading on ground and water systems following an incident that continuously threatens ecosystems and human life for a long time (Vincent et al., 2014).

Cesium isotopes, ^{134}Cs and ^{137}Cs, are of the most concerns due to its large abundance in fission products, its long decay period with a half-life as long as 30.17

years, and its strong radioactivity that emits high-energy gamma rays (Barraqué et al., 2018; Bartonkova et al., 2007). Moreover, because of its similar chemical properties to potassium, it can be readily transferred to biospheres and then causing serious radiological hazards to the environment and human body (Zhang et al., 2020). So far, many methods have been studied to remove Cs^+ in wastewater, including ion exchange, adsorbent sorption, membrane extraction, solvent extraction, reverse osmosis, chemical precipitation,with their purification efficiency varying from each other (Bostick et al., 2002; Yun Kon Kim, 2018).

In fact, quite a number of the purification methods rely on the adsorbents involved and hence development of effective adsorbents is the key. Various Cs^+ adsorbents such as vanadium silicate(Datta et al., 2014), chalcogenides (Ding and Kanatzidis, 2010), zeolite (Borai et al., 2009; Prajitno et al., 2020), clay (Ma et al., 2011), layered double hydroxides (LDHs) (Gu et al., 2018) have been studied and assessed in term of capacity, selectivity and kinetics. Among the adsorbents, analogues of Prussian Blue (PBA) (Delchet et al., 2012), have stood out thanks to its excellent sorption capacity and superior selectivity for Cs^+ even in the background environment with a large quantity of various competing cations, as well as its facile preparation (Turgis et al., 2013; Yang et al., 2016). Potassium copper hexacyanoferrate (KCuHCF) is one of the representative PBA analogs that is of great interest. The KCuHCF has a perovskite-like face-centered cubic crystal structure with a channel diameter approximately 3.2 Å, acting as an ion-sieve specifically for hydrated cesium ions, with Cs^+ capable of permeating the lattice structure but larger competing ions being blocked (Baik et al., 2017; Turgis et al., 2013;

Vincent et al., 2014). However, the extremely small size (~10 nm) of the hexacyanoferrate (HCF) limits its use in practical applications due to the challenging recovery from water and needs to be immobilized on some larger supportting materials, such as mesoporous silica (Causse et al., 2014; Sangvanich et al., 2010), carbon allotropes (Yang et al., 2014a; Yang et al., 2014b), chitin (Vincent et al., 2015; Vincent et al., 2014), alginate (Jang and Lee, 2016; Yang et al., 2014a), etc.

Natural clay minerals have also been demonstrated to be an adsorbent of metal ions and been used to adsorb radionuclides (such as Cs^+, Sr^{2+}, Co^{2+}) (Long et al., 2013; Ma et al., 2011), benefiting from its advantages of large abundance, low cost and environment- friendliness. In particular, montmorillonite (Mt) is one of the most interests among the natural mineral clays. It is a smectite clay composed of two layers of Si^{4+} tetrahedral sheets sandwiching a layer of Al^{3+} octahedral sheets (Yuan et al., 2009). The expandable interlayer including plenty of accumulated cation ions inside endows the Mt with a high cation exchange capacity (CEC) and a strong sorption performance (de Pablo et al., 2011). Hence, the Mt was widely used to adsorb Cs^+, having a maximum capacity reported in the range of 57-104 mg g^{-1} while a very low selectivity towards Cs^+ (Durrant et al., 2018), selectivity values ranging from $10^1 \sim 10^3$ mL/g (Bostick et al., 2002; Deepthi Rani and Sasidhar, 2012). Besides, in light of the stable chemical and mechanical properties and large specific surface area (Wang et al., 2010), Mt has been a good supporting matrix for nanoparticles immobilization and also used as carrier for HCF with enhanced capability to adsorb Cs^+ (Zhang et al., 2017).

Upon removing the Cs^+, recovery of the adsorbent from aqueous environment is needed to avoid a secondary pollution and to facilitate post-treatment of the cesium element. Typical solid-liquid separation methods such as filtration (Kim et al., 2020), centrifugation (Pushkarev et al., 1960), precipitation (Fujita et al., 2014), and flotation (Baik et al., 2017; Kim et al., 2017b), etc., have been reported while often argued to be either inefficient or environment-unfriendly since additional chemicals are required such as flocculants or frothers that further burden the environment. Magnetic separation, mostly using magnetite (Fe_3O_4) nanoparticles, still remains as a simple method to recover adsorbents from wastewater, and is often used in actual wastewater treatment (Kim et al., 2017b).

Indeed, there have been efforts to develop magnetic adsorbents by combining magnetite with nanoparticles of hexacyanoferrate, and have been proved to be a promising method in purifying Cs^+ contaminated water (Hwang et al., 2017; Mobtaker et al., 2016; Roh et al., 2019). It was realized either by directly coating HCF onto magnetite (Hwang et al., 2017) or with the aid of a supporting matrix (Mobtaker et al., 2016; Roh et al., 2019). For instance, Mobtaker et al (Mobtaker et al., 2016) used polyacrylonitrile as a support to hold the magnetite and HCF together and did improve both the adsorption performance and mechanical properties. However, even though magnetic clay has been well studied and demonstrated to be a good magnetic carrier thanks to its large surface area, there has no work yet reported in combining it with HCF for cesium removal.

This study reports the preparation and performance test of magnetic montmorillonite-KCuHCF composite adsorbent. Montmorillonite clay nanosheets are not only a carrier for fixing HCF nanoparticles, but also an adsorbent for Cs. Fe^{2+} was used to replace the ions in the interlayer of the montmorillonite particles before being oxidized to form Fe_3O_4, hence forming a magnetic clay. Dopamine (DOPA) is a natural catecholamine that can self-polymerize to polydopamine (PDOPA) under oxygen and weak alkali (Lee et al., 2007). The PDOPA not only can form an adhesive coating on Mt as similarly sticky as mussels, but also able to complex with Cu^{2+} ions thanks to the amino and catechol groups. The binded Cu^{2+} ions by the PDOPA coated on the magnetic clay surface can act as loci to *in situ* synthesize KCuHCF nanoparticles, so as to immobilize the KCuHCF nanoparticles on the magnetic clays. The composite adsorbent was evaluated in terms of cesium sorption capacity, magnetic recovery and regeneration performance, etc. As compared to other methods such as froth flotation, systems involving hydrogel adsorbents, and that of polymer supported magnetic adsorbents, etc., the new method developed in this study that combines magnetic clay with HCF shows advantages including easy-use and environmental friendliness requiring no additional chemicals, good mechanical performance with potential radiation resistance, and low cost, etc.

2. EXPERIMENTAL

2.1 Chemicals

Montmorillonite powder (specific surface 240 m^2/g), dopamine hydrochloride (>99.8%) and tris (hydroxymethyl) aminomethane (>99.9%, $C_4H_{11}NO_3$, TRIS) were obtained from Macklin, and used directly. Cesium chloride (CsCl, analytical grade), potassium hexacyanoferrate (>98%, $K_4[Fe(CN)_6]\cdot 3H_2O$), and copper sulfate (>99%, $CuSO_4\cdot 5H_2O$)were obtained from Sigma-Aldrich, and used without further treatment. Ferrous sulfate (>98%, $FeSO_4\cdot 7H_2O$) , potassium nitrate (>99%, KNO_3) , Hydrogen peroxide ((30%, H_2O_2), Hydrazine Hydrate (80%, N_2H_4) were acquired from Sinopharm Chemical Reagent Co, Ltd.

2.2 Synthesis

2.2.1 Preparation of montmorillonite suspension

30g of montmorillonite were dispersed in 1L of ultrapure water (resistivity of 18.2 MΩ.cm), stirred gently for 3 hours, and allowed to stand for 12 hours. The supernatant liquid was decanted to obtain smaller particles and to remove any potential sands (e.g. magnetite), and stored for later use.The particle concentration in the collected supernatant liquid was determined by dry mass measurement.

2.2.2 Preparation of magnetic montmorillonite

Magnetic montmorillonite (Mt-Mag) was prepared by a low-temperature hydrothermal method, following the reference (Bartonkova et al., 2007), with the synthesis shown by the reaction scheme below. First, 5 mL of $FeSO_4\cdot 7H_2O$ (0.3 M) and 85 mL montmorillonite suspension (1.3647 g/L) were mixed and kept stirring at room temperature for 2 h, allowing Fe^{2+} to replace the cations in the interlayer of montmorillonite. Then 5 mL KNO_3 (0.49 M) was added dropwise, followed by the addition dropwise of 5 mL KOH (1.25 M), wherein the suspension turned green, and the mixture was kept stirring and heated up to 90 °C allowing the reaction to happen for some time until the color became dark brown, indicating the formation of magnetic montmorillonite. Afterwards, the mixture was cooled to ambient temperature under stirring, then washed twice with ultrapure water. The resultant clean magneticmontmorillonite was collected by magnetic force and re-dispersed to 100 mL with ultrapure water. The solid content of Mt-Mag suspension is 2.03 g/L.

$$3FeSO_4 + 4KOH + 2KNO_3 = Fe_3O_4 + 2NO_2 \uparrow + 2H_2O + 3K_2SO_4$$

2.2.3 Preparation of polydopamine coated magnetic montmorillonite (D-Mt-Mag)

121.14 mg TRIS was mixed with 50 mL Mt-Mag suspension (2.03g/L) under stirring to obtain pH 8.5, then 161.51 mg DOPA·HCl (i.e. 130.42 mg DOPA) was loaded to the system, and the system was kept stirred for 2 h, following a protocol reported in an earlier study (Zhang et al., 2020). When DOPA was added to the Mt suspension, the color of the suspension experienced a gradual change from brown to black. The product was magnetically separated from liquid and rinsed with ultrapure water 3 times to remove the excess unreacted DOPA and uncoated polydopamine. Pure PDOPA sample was made as a control sample in ultrapure water but in the absence of Mt-Mag under identical experimental conditions.

2.2.4 Preparation of composite adsorbent

The D-Mt-Mag-HCF composite adsorbent was fabricated by a multi-step routes from Mt suspension (see Fig. 1). When the PDOPA coated magnetic Mt (D-Mt-Mag) was obtained after the first two steps, the particles were loaded in a polypropylene centrifuge tube (50 mL) and re-dispersed with 10 mL ultrapure water, then 10 mL 0.5

M $CuSO_4$ solution was added, and shaken in an orbital shaker (200 rpm) for 12 hours to allow the coated PDOPA on clay to chelate Cu^{2+} ions. The suspensions were then separated with a magnet, and washed with ultrapure water to remove the excess Cu^{2+} ions. Afterwards, 10 mL ultrapure water was used to re-disperse the particles, then 10 mL 0.5 M $K_4Fe(CN)_6$ (KHCF as abbreviation) was added and stirred in the orbital shaker (200 rpm) for 12 hours, whereby the KHCF was expected to react with the chelated Cu^{2+} ions to *in situ* generate KCuHCF nanoparticles on the magnetic clays, with the composite named D-Mt-Mag-HCF. The product was separated with a magnet and rinsed with ultrapure water 3 times to remove the excess unreacted KHCF. The D-Mt-Mag-HCF composite adsorbent were stored wet (12.47 g/L) to avoid the problems of particle agglomeration and re-dispersion, facilitating the subsequent cesium sorption experiments.

For the sake of comparison in terms of sorption capacity, non-magnetic composite adsorbent D-Mt-HCF was prepared under identical conditions based on Mt suspension.

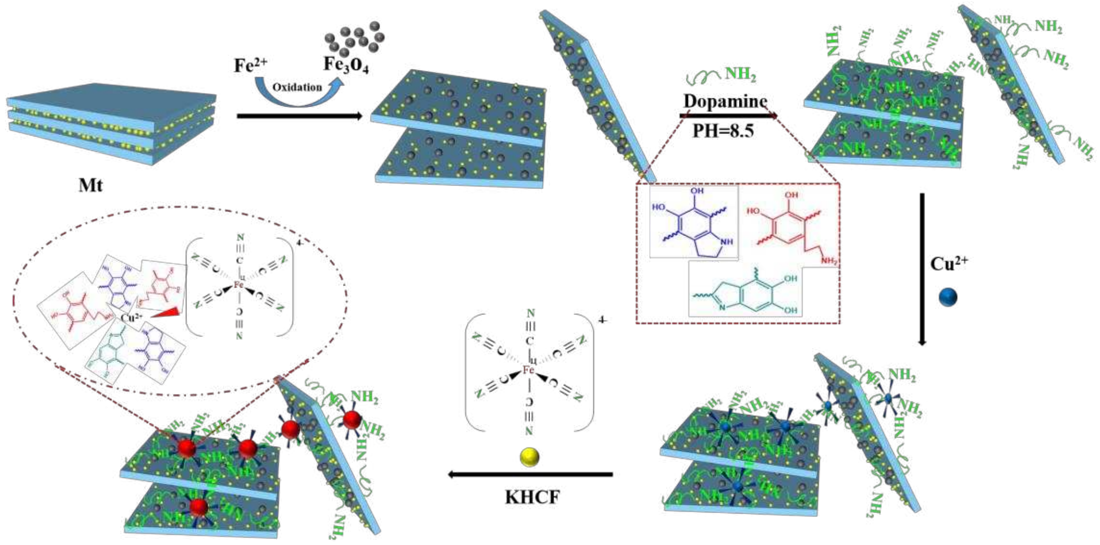

Figure 1. Schematic of the multi-step synthesis route of D-Mt-Mag-HCF composite adsorbent from Mt suspension.

2.3 Materials Characterization

2.3.1 Fourier Transform Infrared (FT-IR): To determine the chemical composition and functional groups, the specimens were analyzed using Fourier transform infrared spectroscopy (FTIR, Nicolet 5700) through the KBr tablet method within the wavelength range of 400~4000 cm^{-1}.

2.3.2 X-ray Photoelectron Spectroscopy (XPS): Thermo K-Alpha XPS system sourced with a monochromatic Al Kα X-ray was used to analyze the chemical bonds of the samples. The charge accumulated on the sample during the measurement was compensated based on electron/ion gun. The CasaXPS software was used to fit the XPS peak and correct the binding energy refering to the C 1s at 284.5 eV.

2.3.3 Thermogravimetric Analysis (TGA): The sample was characterized by a Mettler-Toledo TGA instrument. The temperature was increased from 30 ℃ to 800 ℃ and the heating rate was 10 ℃/min, nitrogen was used as the protective atmosphere, and the atmosphere rate was 50 mL/min.

2.3.4 Powder X-ray Diffraction (p-XRD): The sample was characterized by X'Pert PXRD X-ray diffractometer from PANalytical, Netherlands. In the p-XRD instrument, X-rays were emitted by a diffractometer with a Cu target (1.54 Å) and received by a LynxEye detector, and worked under 40 kV and 40 mA conditions. The scanning 2θ angle was ranged from 5° to 65° with a step size of 0.03299° at 2 s/step. The composite adsorbent was dried under vacuum (pressure <10 kPa) at 50 °C for 24 hours before being ground into powder for characterization.

2.3.5 Inductively Coupled Plasma-Optical Emission Spectroscopy (ICP-OES): ICP-OES (Optima 8000, Singapore, PerkinElmer) was employed to determine the metal content in the composite adsorbent. Before measurement, the D-Mt-Mag-HCF composite adsorbent was dissolved in a mixture of nitric acid (HNO_3)/ hydrochloric acid (HCl) (3/1 vol/vol) using a microwave digester. The sample solution was scanned at multiple wavelengths, with the element concentration detected at specific wavelengths (Na-589.592 nm, K-769.897 nm, Cu-327.395 nm, and Fe-238.204 nm).

2.3.6 Field Emission Scanning Electron Microscope (FE- SEM): The morphology of the Mt and D-Mt-HCF samples were observed with a Japanese Regukus 8100 cold FE-SEM. The samples were sprayed with gold before the observation. The accelerating voltage was 5.0 kv and the current was 10 uA. The D-Mt-Mag-HCF sample, having magnetic properties, was observed with a German Zeiss Sigma 300 cold FE-SEM. Similarly, the sample was sprayed with gold before the observation, and the accelerating voltage was in the range of 0.02-30 kV, with 10 V step-by-step continuously adjustable, and the probe beam current was in the range of 3pA-20nA, with a stability better than 0.2%/h.

2.4 Cesium Sorption

Cesium (Cs-133) chloride was dissolved in deionized water to simulate radioactive wastewater containing Cs^+ ions. All the sorption experiments were performed in plastic bottles to prevent silicon pollution as well as potential Cs^+ sorption in glassware, as did in previous study (Bostick et al., 2002). The solid content of the adsorbent (e.g. the D-Mt-Mag-HCF composite) was fixed at 1 g/L with a total liquid volume of 16 mL as prepared individually in polypropylene centrifuge tubes. The Cs^+ concentration in the solutions was varied from 10 ppm to 500 ppm, as obtained by dilution from 1000 ppm of Cs^+ stock solution. Note that the experimental concentration scale might be higher than real environmental levels, but still represents reasonability. This is due to the fact that the adsorbents are subjected to continuing long-term increases in Cs^+ uptake in environment while having a possibly similar mechanism to lab-scale experiment (to accelerate the kinetics)(Fuller et al., 2015) [*A.J. Fuller et al. / Applied Clay Science 108 (2015) 128–134*]. The polypropylene centrifuge tubes with the mixtures were shaked using an orbital shaker (200 rpm) for 24 hours. Afterwards, the sample tube was centrifuged at a speed of 11,000 rpm for 15 minutes, and the supernatant was decanted and filtered with a 0.45 um syringe filter. Both the Cs^+ concentrations in the supernatant and that in the initial solution before sorption were measured by ICP-OES, a tool widely used for cesium measurement in earlier studies(Park et al., 2010; Xu et al., 2021)[*L. Xu et al. Solid State Ionics,2021, 361,115551; Y. Park et al. Chemical Engineering Journal,2010,162, 685–695*]. It is noted that since the most sensitive emission line of Cs at 852.12nm is overlapped by an emission line of plasma gas of argon at 852.14nm, a wavelength of 894.347 nm was used in ICP-OES to maximize the measurement sensitivity. Moreover, before each measurement a calibrataion was made first using a CsCl standard solution with a known concentration of 0.1 to 10 ppm.

The amount of Cs^+ sorbed by the adsorbent, *q* (mg/g), was determined based on following equation:

$$q = \frac{(C_O - C_e)V}{m} \qquad (1)$$

Here C_o and C_e are the initial and equilibrium concentration (mg/L) of Cs^+ in the solution, determined by ICP-OES, V (L) represents the suspension volume and m (g) is the adsorbent mass, respectively.

The measurement of sorption kinetics was based on a fixed C_o of 100 ppm and the sorption time was varied from 10 minutes to 24 hours. All the sorption experiments were carried out under neutral pH condition, excluding the study of pH effect. The study on the pH dependence of the sorption was performed at a pH range of 2 to 12 with a fixed C_o equal to 300 ppm. The pH of the solution was corrected with 1.0 M HCl and/or 1.0 M KOH solutions, and the other conditions remained the same as previously described (that is, the solid/liquid ratio is 1g/ L , shaken at 300 rpm for 24 h). In order to study the selective sorption of Cs^+ under competitive ion conditions, the composite adsorbent (1 g/L) was dispersed in 20 mL of brine solutions with varied K^+ concentrations, containing 10 ppm Cs^+ for sorption test. The sample was shaked for 24 hours, then the supernatant was separated, and the Cs^+ concentration was measured by ICP-OES, being diluted to the range of 0.1-10 ppm before measurement.

2.5 Regeneration of the composite adsorbent

To evaluate the regeneration feasibility of the adsorbents, the Mt, D-Mt-Mag, D-Mt-Mag-HCF were first subjected to Cs^+ sorption at a fixed C_0 of 300 ppm (solid/liquid ratio: 1g/L; shaking at 200 rpm) for 24 hours to reach an sorption saturation. Subsequently, the adsorbents were washed with ultrapure water, before being soaked in

5 M H_2O_2 solution, at a solid/liquid ratio of 4 g/L, to allow for any potential oxidation reaction for 10 hours. The Cs^+ concentration in the solution as released from the adsorbent was measured by ICP-OES. Afterwards, the adsorbents were washed with ultrapure water and reduced using N_2H_4. The concentration of N_2H_4 solution used was 4 M, and the solid-to-liquid ratio was 4 g/L, and the reaction was allowed to last for 10 hours. The regenerated adsorbent was washed with ultrapure water and used to re-adsorb Cs^+ at a C_0 of 300 ppm. The sorption capacity of the regenerated adsorbent was determined based on the reduction of the Cs^+ concentration in the solution as analyzed by ICP-OES.

3. RESULTS AND DISCUSSION

3.1 Fabrication and characterization of D-Mt-Mag-HCF composite adsorbent

To fabricate a composite adsorbent that owns a superior Cs^+ removal performance and able to be magnetically recovered, a successive four-steps route was employed, starting with growth of magnetite within clay to make the adsorbent magnetic, before coating with polydopamine–to complex Cu^{2+} for subsequent immobilization of KCuHCF nanoparticles to achieve a superior Cs^+ adsorption capacity. In particular,~~First,~~ magnetic montmorillonite was first synthesized following the low-temperature hydrothermal method, and then dopamine was self-polymerized to coat the surface of Mt-Mag. Mixing with $CuSO_4$, the PDOPA on Mt-Mag was complexed with Cu^{2+} (likely via the amino groups), acting as binding sites to react with $K_4Fe(CN)_6$ to form KCuHCF nanoparticles *in situ*. The resulting magnetic composite adsorbent is referred to as D-Mt-Mag-HCF. The four-step fabrication route for D-Mt-Mag-HCF from Mt is shown in Figure 1.

Fig. 2a shows the XRD patterns of D-Mt-HCF, D-Mt-Mag and D-Mt-Mag-HCF with those of Mt, KCuHCF and Fe_3O_4 (Mag) also shown as reference. The pristine Mt has a basal plane (d_{001}) spacing of 1.51 nm, as determined from the diffraction peak (2θ) at 5.81°. For the non-magnetic D-Mt-HCF, the interlayer spacing (d_{001}) was similar, while for the magnetic D-Mt-Mag and D-Mt-Mag-HCF, the diffraction peak of (001) was almost disappearing, if not, shifting to a very low angle. This indicates an interlayer intercalation, expansion and (partial) exfoliation of clay lump along with the formation and growth of magnetite in clay. The characteristicpeaks at 2θ of ~30°, 35° and 57° for D-Mt-Mag-HCF and D-Mt-Mag can be assigned to the (220), (311) and (511) planes of the Fe_3O_4 crystal structure (JCPDS card no. 01 - 1111), confirming the presence of Fe_3O_4 nanoparticles. In addition to the characteristic peaks of Mt centered at 2θ of 19.8°(020), 61.8°(-332) (JCPDS card no. 58-2038), both D-Mt-Mag-HCF and D-Mt-HCF show characteristic peaks centered around 2θ of 17.7°, 25° and 36° (somewhat overlapping with that of Fe_3O_4), which can be attributed to the (200), (220) and (400) planes of the KCuHCF crystal structure (a cell constant of 9.99 Å; JCPDS card no. 02-0383 for $K_2Cu\ [Fe(CN)_6]$) (Qu et al., 2011). Thus, the XRD data validates the formation of magnetic Mt and the existance of KCuHCF within the clay matrix (D-Mt-Mag-HCF).

Moreover, the nanoparticle size of KCuHCF in D-Mt-mag-HCF is likely estimated using the Scherrer equation:

$$L = \frac{K\lambda}{\beta \cos\theta} \qquad (2)$$

where *K* is the dimensionless factor of the crystal shape, considered as 0.94 (Turgis et al., 2013), λ represents the X-ray wavelength (CuKα is 1.5406 Å), β represents the full-width-at-half-maximum height (FWHM, rad) and θ represents the diffraction angle of the peak (rad). Based on the major peaks at 17.7° and 25°, the average particle size of KCuHCF in D-Mt-Mag-HCF was approximately 13.76 nm. Likewise, the size of magnetite particles was estimated from Scherrer equation based on the characteristic peaks (i.e. 30°, 35° and 57°) of Fe_3O_4 to be ~15.3 nm for that formed in D-Mt-Mag-HCF and ~14.6 nm for that in D-Mt-Mag.

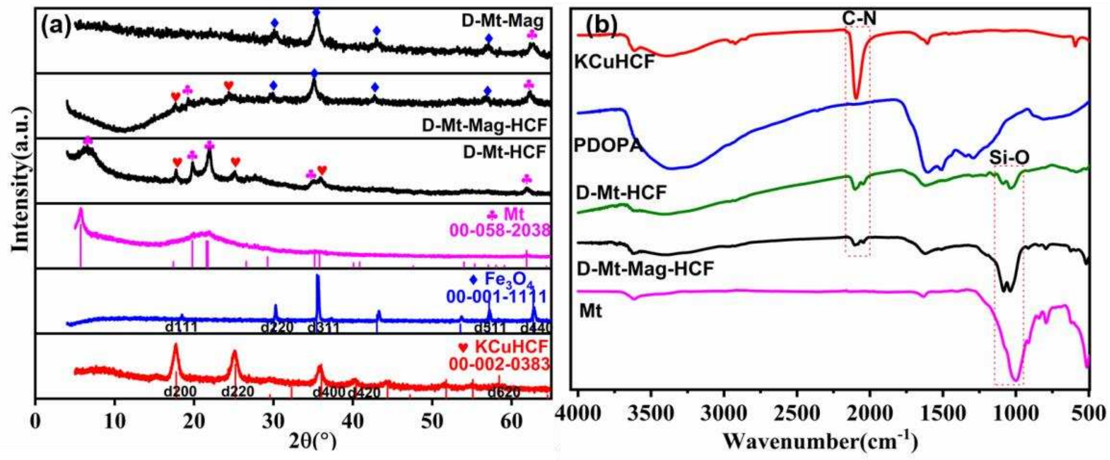

Figure 2. (a) p-XRD patterns of Mt, KCuHCF, Fe_3O_4 (Mag), D-Mt-HCF and D-Mt-Mag-HCF. The pattern files of Mt (JCPDS-ICDD00-058-2038), KCuHCF (JCPDS-ICDD 00-002-0383), Fe_3O_4 (JCPDS-ICDD 00-001-1111) are shown for reference; (b) FTIR spectra of Mt, PDOPA, KCuHCF, D-Mt-HCF and D-Mt-Mag-HCF.

FTIR spectroscopy was used to qualitatively verify that: i) PDOPA was successfully coated on Mt; and ii) KCuHCF nanoparticles were well synthesized. Fig. 2b compares the FTIR spectra of pure-PDOPA, pure-KCuHCF, pristine-Mt as well as the composite adsorbents of D-Mt-HCF and D-Mt-Mag-HCF. Compared with pristine-Mt, D-Mt-HCF and D-Mt-Mag-HCF exhibited new peaks/bands, for example the wide adsorption band between 3100-3500 cm^{-1}, caused by the abundant hydroxyl and aminol groups on the surface, and a peak at 1630 cm^{-1} which is assigned to the aromatic rings of PDOPA (Fei et al., 2008; Yang et al., 2011), confirming the coating PDOPA on Mt. The PDOPA coating is thought to occur between the catechol groups of PDOPA and the silanol groups on the Mt surface, which resulted in slightly shifting the peak at ~1100 cm^{-1} (to higher wave numbers and/or peak splitting), which corresponds to the Si–O vibration of the tetrahedral silica in Mt. Furthermore, for D-Mt-HCF and D-Mt-Mag-HCF, a new peak at 2073 cm^{-1} assigned to the stretching vibrations of CN (Kim et al., 2017a; Turgis et al., 2013; Yang et al., 2014b) confirms the generation of the ferrocyanide structure and the good presence of KCuHCF nanoparticles in D-Mt-HCF and D-Mt-Mag-HCF.

The synthesis steps of the D-Mt-HCF and D-Mt-Mag-HCF was further confirmed by XPS, using pristine-Mt and KCuHCF as reference (Fig. 3). The survey spectra showed an N 1s peak emerged in D-Mt compared to pristine-Mt, proving the coating of PDOPA on Mt surface. When compared to D-Mt, peaks of Fe(2p), K(2p) and Cu (2p) were identified in the survey spectra of D-Mt-HCF and D-Mt-Mag-HCF, and the intensity of the N 1s peak was increased, confirming the existance of KCuHCF nanoparticles (Fig.3a) in the composite.

To reveal interactions between the components (e.g. PDOPA, KCuHCF, Fe_3O_4) in the composite, high-resolution XPS spectra of N 1s, Cu 2p, and Fe 2p (Figs. 3b, c, and d, respectively) were used to analyze chemical bonds. The deconvolution of the N 1s peak (Fig. 3b) showed the D-Mt-Mag-HCF had similar deconvoluted peaks with D-Mt-HCF, implying the PDOPA coating was not affected by the presence of Fe_3O_4 in the interlayer of Mt. The peaks at 399.01 eV, 399.36 eV and 401.47 eV can be assigned to pyridinic N (-N = C-), pyrrolic N (R-NH-R or indole groups) and primary amine or its protonated form (i.e. nitrogen ($R\text{-}NH_2/R\text{-}NH_3^+$)), respectively (Tawil et al., 2013; Yang et al., 2011). The presence of pyridine dinitrogen and pyrrole nitrogen confirms the self-polymerization of dopamine to PDOPA, the primary amine is considered to originate from non-covalently self-assembled dopamine existing within the covalently-polymerized PDOPA (Gao et al., 2013). Note that the higher amount of pyridinic *N* than pyrrolic *N* here is consistent with some earlier studies (Han et al., 2019; Niu et al., 2012)(Niu et al. 2012; Han et al. 2019). However, it is still difficult to explain the exact reason since the mechanism of dopamine oxidative polymerization into PDOPA remains elusive(Liu et al., 2014) (Liu et al. 2014), but it is supposed to be associated with the reaction condition and oxidation degree. Moreover, a characteristic peak at 400.68 eV was observed in both the magnetic and non-magetic composites, and identifies the chelation of amine groups with Cu^{2+} (Fig. 1), contributing to the *in situ* growth of KCuHCF nanoparticles and their immobilization on Mt. The amine groups coordinating with Cu^{2+} include those from PDOPA and the cyano group from KHCF (the precursor of KCuHCF), which can simultaneously coordinate with a single Cu^{2+}.

This is due to the slightly distorted octahedral geometry of the Cu-amine complex, and one of the amine ligands is labile that is likely displaced by the cyano group in the ferrocyanide anion of KHCF (Fig. 1). In addition, a strong peak was observed at 397.17 eV in D-Mt-HCF and D-Mt-Mag-HCF (Fig. 3b), and is ascribed to the CN group ($[Fe(CN\ )_6]^{4-}$), further confirming the existance of KCuHCF nanoparticles in the composite materials. Moreover, the D-Mt-Mag-HCF has a higher peak intensity than D-Mt-HCF, indicating a greater amount of HCF being formed in the presence of magnetite.

The Cu $2p^{3/2}$ spectrum in Fig. 3c confirms the chelation of copper (II) with amino groups and catechol in D-Mt-Mag-HCF and D-Mt-HCF. Compared with D-Mt, D-Mt-Mag-HCF and D-Mt-HCF have characteristic peaks at ~932 eV, which is caused by the redox reaction of Cu^{2+} chelated with amino and catechol groups. In addition, the peak intensity in D-Mt-Mag-HCF and D-Mt-HCF is greater than pure KCuHCF as in the latter Cu^{2+}-N≡C chelation only happens within the KCuHCF complex itself.

The deconvolution of the Fe 2p peak (Fig. 3d) represents two different oxidation states of Fe^{2+} (708.65 and 721.45 eV) and Fe^{3+} (710.15 and 724.51 eV) (Wei et al., 2015). Compared with KCuHCF, D-Mt-Mag-HCF exhibits higher intensity Fe^{3+} peaks, which is related to the presence of Fe_3O_4. The subtle peaks of Fe^{3+} observed at ~723 eV and ~710 eV in KCuHCF indicates a partial oxidation of Fe^{2+}, while most of Fe in the KCuHCF particles exists in term of Fe^{2+} state.

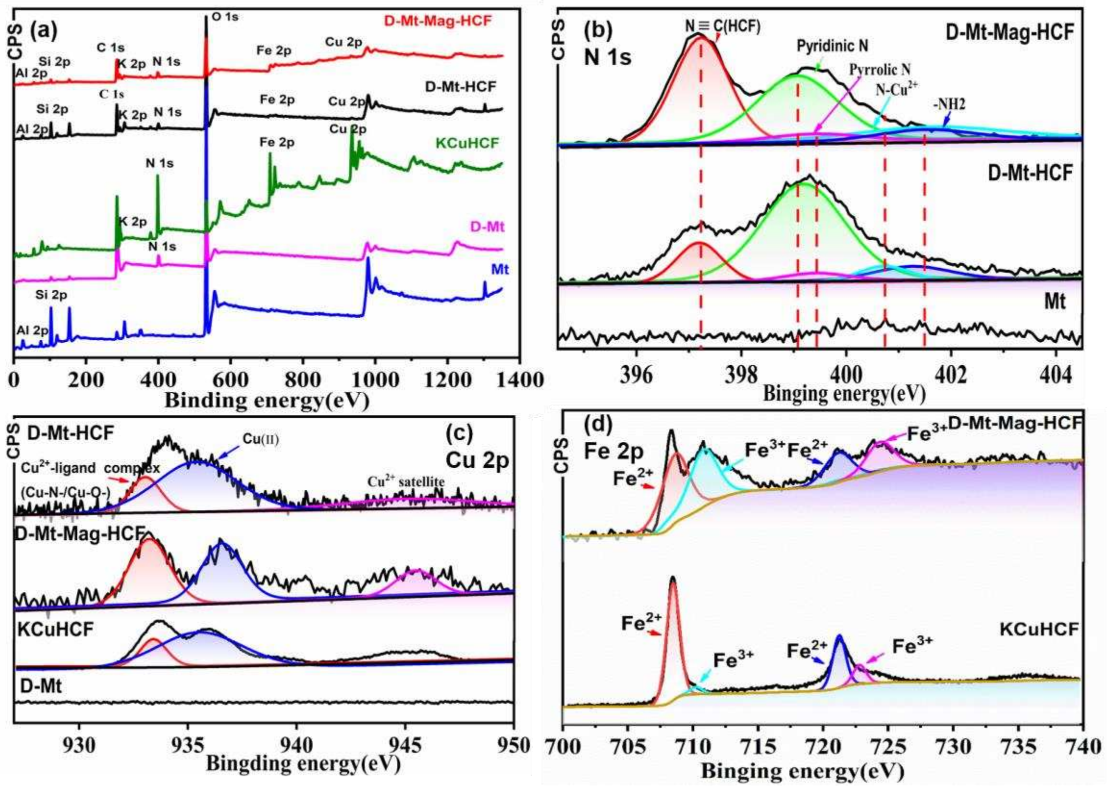

Figure 3. (a) XPS survey spectra of D-Mt, D-Mt-Mag-HCF and D-Mt-HCF with KCuHCF and Mt as references. (b) High-resolution XPS spectra of N 1s peaks of D-Mt, D-Mt-Mag-HCF and D-Mt-HCF with Mt as a reference (the dotted line is used as a guide for the eyes). (c) High-resolution XPS spectra of Cu 2p peaks of D-Mt, D-Mt-Mag-HCF and D-Mt-HCF, KCuHCF. (d)) Fe2p spectra of D-Mt-Mag-HCF and KCuHCF.

Using pristine-Mt as the control sample, the metal content in D-Mt-Mag-HCF and D-Mt-HCF was determined using ICP-OES (Table 1). The stoichiometric chemical composition of KCuHCF is set to $K_{4x-2}Cu[Fe(CN)_6]_x$ (Kim et al., 2017b; Kim et al., 2017c). Based on the measured K/Cu molar ratio, and the stoichiometric charge balance, the form of KCuHCF incorporated in D-Mt-Mag-HCF was estimated to be $K_{0.91}Cu[Fe(CN)_6]_{0.73}$, and the form of KCuHCF incorporated in D-Mt-HCF was estimated as $K_{0.33}Cu[Fe(CN)_6]_{0.58}$, both being consistent with published structures (Vincent et al., 2014). Note that the negligible Fe detected in pristine Mt should not originate from magnetite sand as it was excluded from the XRD spectrum of Mt, but probably existing as counter ions in the interlayer.

From the estimated composition, determining the mass ratio of KCuHCF in the composite material is not trivial and found to be 13.68 wt% in D-Mt-Mag-HCF and 7.23 wt % in D-Mt-HCF. The difference is probably due to the presence of Fe_3O_4 that expanded the interlayer of Mt and/or even partly exfoliated the Mt thus increasing the surface area and favoring the loading of PDOPA and HCF nanoparticles. The Fe_3O_4 amount was estimated to be ~35.09 wt% in the D-Mt-Mag-HCF.

Table 1. Metal content of Mt, D-Mt-HCF and D-Mt-Mag-HCF determined by ICP-OES.

Sample	**Cu (mmol/g)**	**Fe (mmol/g)**	**K (mmol/g)**
Mt	0.0906	0.0227	---
D-Mt-HCF	0.4919	0.459	0.1207
D-Mt-Mag-HCF	0.6684	4.349	0.4909

The thermal degradation behavior of the samples were studied using TGA under N_2 atmosphere. As shown in Fig. S1, the pure materials (Mt, PDOPA and KCuHCF) and composite materials (D-Mt-Mag-HCF and D-Mt-HCF) exhibited different degrees of degradation in the temperature range 30 to 700°C. For Mt, the subtle mass loss with increasing temperature can be ascribed to dehydroxylation of the aluminum-silicate layer. For KCuHCF, the mass loss below 200°C relates to decomposition of cyano groups and the removal of coordination water, with the gradual mass loss at higher temperatures likely due to oxidative decomposition of iron oxide (Yu et al., 2017). As an organic component, PDOPA showed good thermal stability with only ~40 wt% mass loss at 700°C, which is ascribed to its carbon-yielding characteristic similar with a phenolic resin (Hassan et al., 2019; Lee et al., 2013).

From the TGA data of the pure and composite materials, it is possible to approximate the mass (wt %) of the different components in the composite materials, see Supporting Information for further details. For instance, in D-Mt-Mag-HCF, the proportion of KCuHCF was estimated to be 18.1 wt%, assuming the composite material was composed of D-Mt-Mag and KCuHCF, which undergoes identical decomposition kinetics to the individual components. This approximation is consistent with that determined by ICP-OES, considering the difference in techniques.

Using SEM, the morphology of pristine-Mt, D-Mt-Mag-HCF and D-Mt-HCF are compared in Fig. 4, with SEM images of D-Mt-Mag and the corresponding EDX images of D-Mt-HCF provided in the Supporting Information (Fig. S2). The surface area of clay platelets were measured to be 1.81±0.85 μm^2, 1.36±0.70 μm^2 and 1.56±0.10 μm^2 for Mt, D-Mt-HCF and D-Mt-Mag-HCF, respectively. One more interesting thing is that the clay platelets in D-Mt-Mag-HCF(e-f) and in D-Mt-Mag(Fig.S2a-b) were much thinner than that in D-Mt-HCF(c-d) and in Mt(a-b), which were considered to be a result of interlayer intercalation, expansion and exfoliation of clays by the formed magnetite. This can favor immobilization of HCF nanoparticles in light of the increased surface area. Moreover, when compared with pristine-Mt, the composite materials clearly show particle clusters coated on the clay platelets of Mt, albeit the coverage is nonuniform. These nanoparticles are KCuHCF in D-Mt-HCF, magnetite in D-Mt-Mag and mixture of both in D-Mt-Mag-HCF. The presence of KCuHCF nanoparticles in the D-Mt-Mag-HCF was confirmed by EDX analysis (Fig. S2c-d), with those regions of the particle clusters showing significant Cu element that can be ascribed to KCuHCF. Moreover, the size of the nanoparticles was consistent with the estimation from XRD data, considering the difference between two techniques.

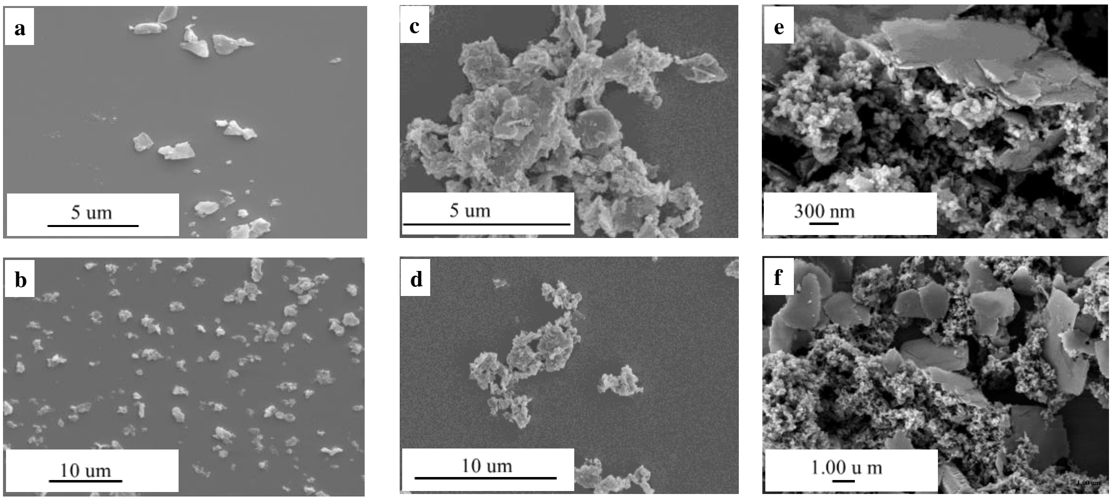

Figure 4. SEM images of Mt(a-b) , D-Mt-HCF(c-d), and D-Mt-Mag-HCF(e-f)

3.2 Cesium Sorption

The ability to remove cesium from contaminated water was compared for the magnetic composite adsorbent, D-Mt-Mag-HCF, non-magnetic composite D-Mt-HCF, magnetic clay D-Mt-Mag and pristine-Mt. The data is compared for batch sorption studies using a constant mass of adsorbent 16 mg, volume of contaminated water 16 mL and varying the concentration of Cs^+ between 10 and 100 mmol/L. The sorption isotherms (in terms of q in mg g^{-1} vs. the equilibrium concentration (C_e, ppm) of Cs^+) are shown in Fig. 5a. All data were fitted using the reputed Langmuir isotherm, which considers i) surface monolayer sorption, ii) finite binding site number, iii) uniform sorption energy, and iv) no migration of adsorbate on the surface, and is given by:

$$\mathrm{q} = \frac{\mathrm{b}q_{mC_e}}{1+\mathrm{b}C_e} \qquad (3)$$

where b is the Langmuir constant associated with the affinity coefficient (L mg^{-1}) of the binding site, and q_m is the maximum sorption capacity of Cs^+.

As can be seen in Fig. 5a, the Langmuir isotherm well describe the Cs^+ sorption data with great correlation coefficient (R^2) values, which are listed in Table 2 together with the fitting parameters (q_m and b) for each adsorbent. Both D-Mt-HCF and D-Mt-Mag-HCF show excellent sorption performance, with q_m values of 143 mg/g and 159.2 mg/g, substantially better than pristine-Mt and D-Mt-Mag which have q_m values of ~60 mg/g and ~30 mg/g. The sorption data further confirms the successful inclusion of KCuHCF nanoparticles in the composite adsorbents, resulting in enhanced Cs^+ sorption capacity. The lower sorption capacity of D-Mt-Mag than pristine-Mt confirmed the successful intercalation of magnetic nanoparticles (Fe_3O_4) in the interlayer of Mt, thus lowering the cation exchange capacity of the Mt. However, with the immobilization of HCF nanoparticles, D-Mt-Mag-HCF showed greater sorption capacity than D-Mt-HCF, which is consistent with the composition of KCuHCF in the composite, as identified by the ICP-OES (Table 1) having more K^+ in D-Mt-Mag-HCF than D-Mt-HCF, as well as more KCuHCF immobilized in the former.

Furthermore, with the contribution from multiple (strong) sorption sites, i.e. KCuHCF nanoparticles and Mt, the sorption isotherms for D-Mt-Mag-HCF and D-Mt-HCF adsorbents were fitted using the dual-site Langmuir sorption model, which accounts for two sorption sites of distinct sorption energies. The model is given by:

$$q = \frac{b_1 q_{m1} C_e}{1+b_1 C_e} + \frac{b_2 q_{m2} C_e}{1+b_2 C_e} \qquad (4)$$

where b_1, b_2 are the affinity coefficients (L mg^{-1}), and q_{m1}, q_{m2} are the maximum sorption capacity (mg g-1) of the two sorption sites, respectively.

As shown in Fig. 5a and Table 2, the two-site Langmuir model (dashed line) better describes the sorption behavior of D-Mt-HCF and D-Mt-Mag-HCF, with higher correlation coefficients (R^2) than the single-site Langmuir model, which contrasts D-Mt-Mag and Mt which show better R^2 values for the single-site Langmuir model. This confirms that the HCF nanoparticles (KCuHCF) and Mt in the composite adsorbent provide active sites for Cs^+ sorption.

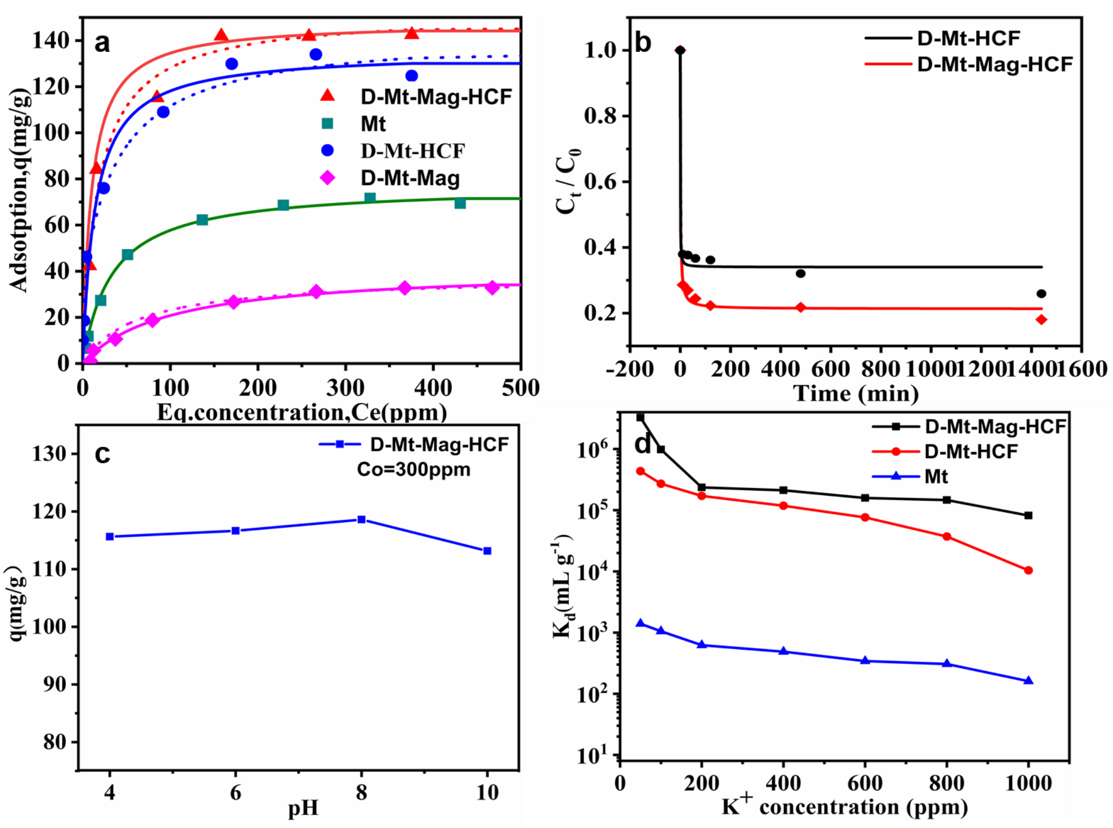

Figure 5. a) Cs^+ sorption isotherm with sorption capacity (q) plotted versus the equilibrium concentration (C_e) for D-Mt-Mag-HCF and D-Mt-HCF, with Mt and D-Mt-Mag as reference. The solid and dashed lines are the fittings of the single-site and dual-site Langmuir models, respectively. b) Cs^+ sorption kinetics of D-Mt-Mag-HCF and D-Mt-HCF at $C_0 = 100$ ppm. c) Cs^+ sorption by D-Mt-Mag-HCF versus the solution pH value ($C_0 = 300$ ppm). d) Distribution coefficient K_d of Cs^+ ($C_0 = 10$ ppm) from potassium (K^+) brine versus K^+ concentration for D-Mt-Mag-HCF and D-Mt-HCF , with Mt as reference.

Since the presence of magnetite enabled an increment in clay surface area and increased immobilization of KCuHCF nanoparticles, and hence one would expect that there existed a specified concentration range of magnetite, within which more magnetite might result in more HCF for Cs retention and better magnetic properties. For comparison purpose, D-Mt-Mag-HCF samples with a lower and a higher Mag/Mt mass ratio (i.e. 0.63 and 2.52) than the focused sample (i.e. a ratio of 1.26) were prepared. The comparisons of their Cs^+ adsorption capacity at C_0 = 20 ppm and C_0 = 300 ppm and their magnetic separation ability are shown in Figure S3 in the Supporting Information. As shown, the low Mag/Mt mass ratio (i.e. 0.63) was insufficient to afford an acceptable magnetic performance albeit it offered a comparable Cs^+ adsorption capacity. The high Mag/Mt mass ratio (i.e. 2.52) provided a good magnetic performance while was lessened in Cs^+ adsorption capacity. Hence, the ratio of 1.26 was in the optimized range that compromised the Cs^+ adsorption capacity and magnetic separation performance.

Table 2. Fittings of Cs^+ sorption by single-site and dual-site Langmuir isotherm models

	Langmuir			**Dual-site Langmuir**				
Adsorbent	**q_m (mg/g)**	**B (L/mg)**	**R^2**	**q_{m1} (mg/g)**	**b_1 (L/mg)**	**q_{m2} (mg/g)**	**b_2 (L/mg)**	**R^2**
D-Mt-HCF	128.1	5.01	0.919	105.6	0.024	37.4	2.741	0.962
D-Mt-Mag-HCF	159.2	0.1	0.942	60	0.01	92	0.04	0.952
D-Mt-Mag	41.24	0.01	0.990	13	0.01	25	0.02	0.947
Mt	75	0.038	0.98					

Table 3 compares Cs^+ sorption capacity as reported in the current study, to other reported values for magnetic adsorbents based on prussian blue analogues. The magnetic composite adsorbent (D-Mt-Mag-HCF) is found to provide greater capacity than hydrogel-based sorbents, likely due to the successful immobilization of dispersed KCuHCF with the magnetic Mt, offering multiple binding sites for Cs^+.

Table 3. Cs^+ sorption capacity of some recently reported magnetic adsorbents.

Adsorbent	**Method of recovery**	**Support**	**q_m (mg of Cs/g of composite)**	**Solution pH**	**ref / year**
KCuHCF	Magnetic	Hydrogels	82.8	8	Kim et al.(Kim et al., 2017b) /2017
KCuHCF	Magnetic	Magnetic chitosan	136.47	8.3-11	Hyelin Roh et al.(Roh et al., 2019) /2019
KFeHCF	Magnetic	Magnetic $CoFe_2O_4$	178.8	7	Hassan et al.(Hassan and Aly, 2019) /2019
CuHCF	Magnetic	polyacrylonitrile	263.2	7	Mobtaker et al./2016(Mobtaker et al., 2016)
NaCuHCF	Magnetic	magnetite	125	7	Hwang et al./2017(Hwang et al., 2017)
KCuHCF	Magnetic	Magnetic Mt	159.2	7	Current study

3.2.1 Sorption Kinetics. The kinetics of Cs^+ sorption were studied for D-Mt-Mag-HCF and D-Mt-HCF (Fig. 5b). The Cs^+ sorption by both composite materials was fast, reaching equilibrium within 100 min. The sorption kinetics can be quantitatively described by fitting the experimental data with a pseudo-second order rate equation

(PSORE):

$$\frac{\mathrm{t}}{q_t} = \frac{1}{K_2 q_e^2} + \frac{t}{q_e} \qquad (5)$$

where q_t and q_e are the adsorbed Cs^+ quantity (mg/g) at time t and at equilibrium, respectively, and k_2 is a rate constant.

For both D-Mt-Mag-HCF and D-Mt-HCF, the PSORE fits are considered reasonable, with R^2 values > 0.97. The model fitting parameters are listed in Table 4. The data for KCuHCF only, that was reported in an earlier study (Kim et al., 2017a), is also listed for comparison. For the rate constant k_2, both D-Mt-Mag-HCF and D-Mt-HCF exhibit much higher k_2 values than KCuHCF, confirming the rapid sorption kinetics of Cs^+, albeit KCuHCF provides a slightly greater sorption capacity. Eventhough the sorption kinetic of D-Mt-Mag-HCF is slightly compromised relative to D-Mt-HCF, it does provide a higher sorption capacity, hence the magnetic modification does not greatly compromise the overall performance of the magnetically-recoverable adsorbent.

Table 4. Fitting parameters of PSORE for Cs^+ sorption by D-Mt-Mag-HCF and D-Mt-HCF composite adsorbents.

Adsorbent	**k_2 (g mg^{-1} min^{-1})**	**q_e**	**R^2**
D-Mt-Mag-HCF	0.01	78.71	0.99
D-Mt-HCF	0.05	66	0.97
Bulk KCuHCF(19.9 ppm	4.39×10^{-4}	94.37	0.98

Cs^+ in DI water)

3.2.2 pH Effect. Figure 5c shows that the effect of pH on Cs^+ sorption (C_0 = 300 ppm) is negligible for D-Mt-Mag-HCF, and confirms the good stability of the magnetic adsorbent in both acidic and basic conditions.

3.2.3 Competitive Ion Effect. With a similar hydrated ion size as Cs^+ (~0.329 nm), K^+ (~0.331 nm) is a strongly competing ion for Cs^+. The sorption selectivity of D-Mt-Mag-HCF and D-Mt-HCF for Cs^+ (initial concentration = 10 ppm) in the presence of K^+ of varying concentrations was studied, and the data is shown in Fig. 5d. The selectivity of Cs^+ from KCl solutions is determined from the distribution coefficient K_d, which is given as:

$$Kd = \frac{Co - Ce}{Ce} \frac{V}{m} \qquad (6)$$

where C_0 is the initial and C_e is the equilibrium concentrations of Cs^+, V *is* the volume (mL) of solution and m is the mass (g) of adsorbent. As shown in Fig. 5d, the selectivity of Cs^+ by D-Mt-Mag-HCF and D-Mt-HCF is significantly greater than pristine-Mt, with $K_d = 3.2\times10^6$ mL g^{-1} for D-Mt-Mag-HCF, 4.3×10^5 mL g^{-1} for D-Mt-HCF and 1.3×10^3 mL g^{-1} for pristine-Mt when the initial concentration of K^+ was 50 ppm. For increasing concentration of K^+ (up to 1000 ppm), the K_d values for all adsorbents gradually decreased. At an initial concentration of K^+ 1000 ppm, D-Mt-Mag-HCF and D-Mt-HCF continued to show very good selectivity for Cs^+, with K_d values higher than 8.2×10^4 mL g^{-1} and 1.0×10^4 mL g^{-1}, respectively. This excellent selectivity of Cs^+ by the two sorbents can be attributed to the immobilized KCuHCF nanoparticles, with the cubic lattices acting as ion sieves to preferentially uptake Cs^+ and exclude slightly larger ions such as K^+.

Moreover, the effects of storage time of adsorbent and temperature of adsorption experiment on Cs^+ removal performance were evaluated at C_0=20ppm for D-Mt-Mag-HCF, with data shown in Fig. S. As demonstrated, the Cs^+ removal effecicy remained as high as ~100% even with the adsorbent stored more than 10 months and was nearly affected by temperature within the measurement range (i.e. 25-40°C).

3.3 Recovery and Regeneration of the Adsorbent

3.3.1 Magnetic property. Once the Cs^+ is removed from the contaminated aqueous environment, it is essential to recover the adsorbent to avoid any secondary pollution. The D-Mt-Mag-HCF adsorbent exhibited facile recovery using an external magnet (Fig. 6). Here, the hysteresis curve of D-Mt-Mag-HCF using D-Mt-HCF as reference, is measured using a vibrating sample magnetometer (VSM) at ambient conditions. While D-Mt-HCF shows no magnetization, as expected, the D-Mt-Mag-HCF adsorbent shows magnetic hysteresis. The saturation magnetization and coercivity of D-Mt-Mag-HCF were 17.4 emu/g and 9.06 Oe, indicating sufficient magnetism to be easily recovered using an external magnet. The magnetic separation in water was evaluated by dispersing D-Mt-Mag-HCF in 20 mL deionized water and positioning the magnet on the sidewall of the glass vial. The dispersion was agitated for 24 hrs and once the magnet was placed on the sidewall of the glass via, the D-Mt-Mag-HCF particle were immediately attracted to the magnet, leaving a non-turbid aqueous phase, thus demonstrating the very fast and almost complete separation of D-Mt-Mag-HCF from water.

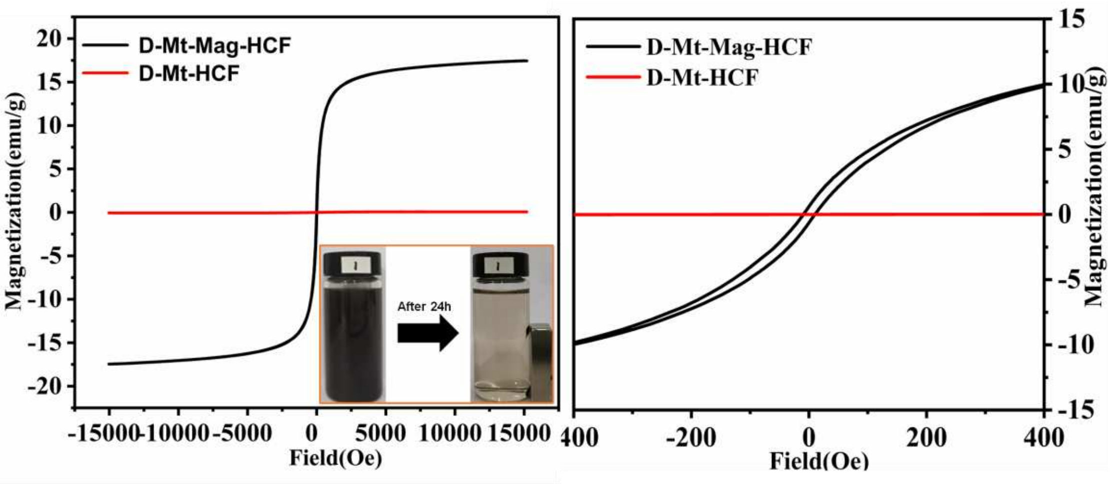

Figure 6. (a) Field-dependent magnetization curves of D-Mt-Mag-HCF and D-Mt-HCF. Inset the photos of D-Mt-Mag-HCF magnetic separation. (b) The central part of the hysteresis loops.

3.3.2 Adsorbents regeneration. Cs^+ desorption to regenerate the adsorbent is vital to extend the lifetime of the adsorbent. It is possible to desorb Cs^+ from metal-hexacyanoferrate (MHCF) through the oxidation of ferrocyanide (A. Nilchi, 2003), as shown in the reaction scheme below. The oxidation reaction can be realized using the oxidant H_2O_2 (H. Won, 2008).

$$Cs_2\,Cu_3[Fe^{II}(CN_6)]_2 4H_2O \xrightarrow{[O]} Cu_3[Fe^{III}(CN_6)]_2 4H_2O + 2Cs^+$$

Following Cs^+ sorption at $C_0 = 300$ ppm, with the sorbed amounts being 68.6 mg/g for pristine-Mt, 31.15 mg/g for D-Mt-Mag, and 141.92 mg/g for D-Mt-Mag-HCF, the adsorbents were subjected to H_2O_2 oxidation, with the amount of Cs^+ desorbed shown in Fig. 7a. As shown, the amount of Cs^+ desorbed is 38.7 mg/g for pristine-Mt, 25.1 mg/g for D-Mt-Mag, and 39.1 mg/g for D-Mt-Mag-HCF, which corresponds to 56.41%, 80.57%, 27.54% Cs^+ desorbed (relative to the total adsorbed amount). The high desorption of Cs^+ from pristine-Mt and D-Mt-Mag is reasonable considering the low selectivity and stability. However, desorption of Cs^+ from D-Mt-Mag-HCF, albeit not complete, shows potential to partially regenerate the adsorbent for continued use.

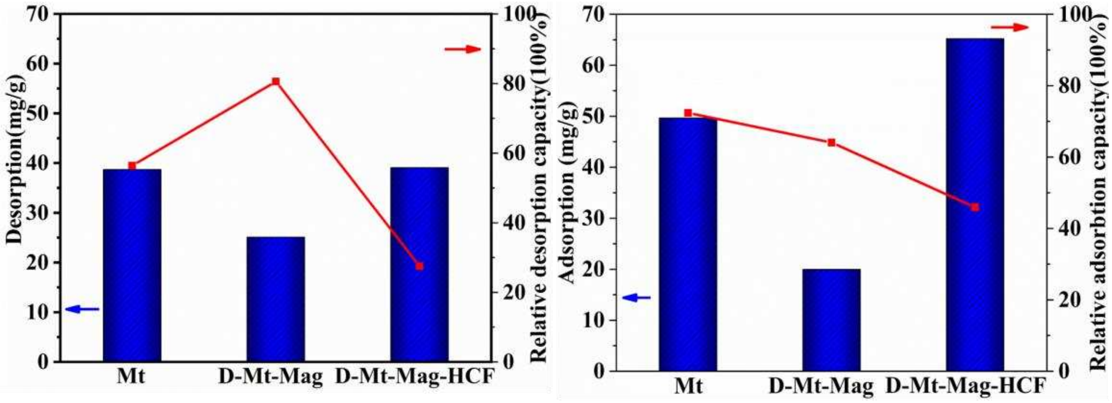

Figure 7. (a) Cs^+ amount in liquid as released from adsorbents via H_2O_2 oxidation and the corresponding relative desorption capactiy. (b) Cs^+ sorption capacity of the used adsorbents after reduction by N_2H_4 and the corresponding ratio to the first sorption capacity.

With the Cs^+ released, the adsorbents were regenerated via N_2H_4 reduction, by reducing Fe^{III} to Fe^{II} in the ferrocyanide, before being used for Cs^+ sorption once more with $C_0 = 300$ ppm. As shown in Fig. 7b, the regenerated adsorbents showed reasonable sorption capacities, with the regenerated D-Mt-Mag-HCF having a capactity up to 67 mg/g which represents ca. 46% of the capacity from the intial sorption test. This method demonstrates the potential to partially regenerate the adsorbent for reuse, although further effort should be given to regeneration the components that strongly and selectively interact with Cs^+.

4. CONCLUSIONS

A magnetic composite adsorbent, D-Mt -Mag-HCF, was successfully prepared based on a Fe_3O_4 intercalated montmorillonite immobilized with potassium copper hexacyanoferrate. The adsorbent was successfully used to decontaminate Cs^+ water before being facily recovered in an applied magnetic field. The synthesis route involved: (i) substitutation of Mt interlayer ions with ferrous ions before transforming to Mt -Mag by low-temperature hydrothermal method; (ii) coating the Mt -Mag with polydopamine to form D-Mt -Mag; (iii) anchoring of Cu^{2+} onto D-Mt -Mag via chelation with the coated PDOPA; and (iv) *in situ* growth of KCuHCF nanoparticles through complexation of the anchored Cu^{2+} with hexacyanoferrate precursor $K_4[Fe(CN)_6]_4$.

The composite adsorbent showed excellent Cs^+ recovery with a maximum sorption capacity of ~159.2 mg/g, and negligible deteriment in changing pH environments. Owing to the incorporation of KCuHCF, the adsorbent provided high selectivity for Cs^+ with a distribution coefficition greater than 8.2×10^4 mL g^{-1} in concentrated brine solutions. More importantly, the composite was magnetically responsive, making it readily recoverable from aqueous environments. Upon recovery, the composite could be partially regenerated for subsequent use.

Acknowledgements

This work was financially supported by the National Natural Science Foundation of China (21903015; 22172028;22111530080), the Natural Science Foundation of Fujian Province of China (2020J01145), and the Award Program of Fujian Minjiang Scholar

Professorship (2018). D.H greatly acknowledges the financial support from the Engineering and Physical Sciences Research Council, UK (Grant No. EP/S032797/1).

References

A. Nilchi, B.M., M. Ghanadi Maragheh & A. Khanchi 2003. Exchange properties of cyanide complexes
Journal of Radioanalytical and Nuclear Chemistry.

Baik, S., Zhang, H., Kim, Y.K., Harbottle, D., Lee, J.W., 2017. Enhanced adsorption capacity and selectivity towards strontium ions in aqueous systems by sulfonation of CO2 derived porous carbon. RSC Advances 7, 54546-54553.

Barraqué, F., Montes, M.L., Fernández, M.A., Mercader, R.C., Candal, R.J., Torres Sánchez, R.M., 2018. Synthesis and characterization of magnetic-montmorillonite and magnetic-organo-montmorillonite: Surface sites involved on cobalt sorption. Journal of Magnetism and Magnetic Materials 466, 376-384.

Bartonkova, H., Mashlan, M., Medrik, I., Jancik, D., Zboril, R., 2007. Magnetically modified bentonite as a possible contrast agent in MRI of gastrointestinal tract. Chemical Papers 61.

Borai, E.H., Harjula, R., Malinen, L., Paajanen, A., 2009. Efficient removal of cesium from low-level radioactive liquid waste using natural and impregnated zeolite minerals. J Hazard Mater 172, 416-422.

Bostick, B.C., Vairavamurthy, M.A., Karthikeyan, K.G., Chorover, J., 2002. Cesium Adsorption on Clay Minerals: An EXAFS Spectroscopic Investigation. Environmental Science & Technology 36, 2670-2676.

Causse, J., Tokarev, A., Ravaux, J., Moloney, M., Barré, Y., Grandjean, A., 2014. Facile one-pot synthesis of copper hexacyanoferrate nanoparticle functionalised silica monoliths for the selective entrapment of 137Cs. J. Mater. Chem. A 2, 9461-9464.

Datta, S.J., Moon, W.K., Choi, D.Y., Hwang, I.C., Yoon, K.B., 2014. A novel vanadosilicate with hexadeca-coordinated Cs(+) ions as a highly effective Cs(+) remover. Angew Chem Int Ed Engl 53, 7203-7208.

de Pablo, L., Chávez, M.L., Abatal, M., 2011. Adsorption of heavy metals in acid to alkaline environments by montmorillonite and Ca-montmorillonite. Chemical Engineering Journal 171, 1276-1286.

Deepthi Rani, R., Sasidhar, P., 2012. Sorption of Cesium on Clay Colloids: Kinetic and Thermodynamic Studies. Aquatic Geochemistry 18, 281-296.

Delchet, C., Tokarev, A., Dumail, X., Toquer, G., Barré, Y., Guari, Y., Guerin, C., Larionova, J., Grandjean, A., 2012. Extraction of radioactive cesium using innovative functionalized porous materials. RSC Advances 2.

Ding, D., Zhang, Z., Lei, Z., Yang, Y., Cai, T., 2016. Remediation of radiocesium-contaminated liquid waste, soil, and ash: a mini review since the Fukushima Daiichi Nuclear Power Plant accident.

Environ Sci Pollut Res Int 23, 2249-2263.

Ding, N., Kanatzidis, M.G., 2010. Selective incarceration of caesium ions by Venus flytrap action of a flexible framework sulfide. Nat Chem 2, 187-191.

Durrant, C.B., Begg, J.D., Kersting, A.B., Zavarin, M., 2018. Cesium sorption reversibility and kinetics on illite, montmorillonite, and kaolinite. Sci Total Environ 610-611, 511-520.

Fei, B., Qian, B., Yang, Z., Wang, R., Liu, W.C., Mak, C.L., Xin, J.H., 2008. Coating carbon nanotubes by spontaneous oxidative polymerization of dopamine. Carbon 46, 1795-1797.

Fujita, H., Sasano, H., Miyajima, R., Sakoda, A., 2014. Adsorption equilibrium and kinetics of cesium onto insoluble Prussian blue synthesized by an immediate precipitation reaction between Fe3+ and [Fe(CN)6]4. Adsorption 20, 905-915.

Fuller, A.J., Shaw, S., Ward, M.B., Haigh, S.J., Mosselmans, J.F.W., Peacock, C.L., Stackhouse, S., Dent, A.J., Trivedi, D., Burke, I.T., 2015. Caesium incorporation and retention in illite interlayers. Appl Clay Sci 108, 128-134.

Gao, H., Sun, Y., Zhou, J., Xu, R., Duan, H., 2013. Mussel-Inspired Synthesis of Polydopamine-Functionalized Graphene Hydrogel as Reusable Adsorbents for Water Purification. ACS Applied Materials & Interfaces 5, 425-432.

Gu, P., Zhang, S., Li, X., Wang, X., Wen, T., Jehan, R., Alsaedi, A., Hayat, T., Wang, X., 2018. Recent advances in layered double hydroxide-based nanomaterials for the removal of radionuclides from aqueous solution. Environ Pollut 240, 493-505.

H. Won, J.-k.M., C. Jung, Won-Yang Chung, 2008. Evaluation of ferrocyanide anion exchange resins regarding the uptake of Cs+ions and their regeneration Chemistry
Nuclear Engineering and Technology.

Han, Y.J., Zhu, Z.J., Huang, L., Guo, Y.J., Zhai, Y.L., Dong, S.J., 2019. Hydrothermal synthesis of polydopamine-functionalized cobalt-doped lanthanum nickelate perovskite nanorods for efficient water oxidation in alkaline solution. Nanoscale 11, 19579-19585.

Hassan, M., Wu, D., Song, X., Ren, S., Hao, C., 2019. Synergistic effect of heat treatment and concentration of polydopamine enhance the electrochemical performances of hollow nitrogen-doped carbon microspheres. Ionics 25, 4685-4701.

Hassan, M.R., Aly, M.I., 2019. Adsorptive removal of cesium ions from aqueous solutions using synthesized Prussian blue/magnetic cobalt ferrite nanoparticles. Particulate Science and Technology 38, 236-246.

Hwang, K.S., Park, C.W., Lee, K.W., Park, S.J., Yang, H.M., 2017. Highly efficient removal of radioactive cesium by sodium-copper hexacyanoferrate-modified magnetic nanoparticles. Colloid Surface A 516, 375-382.

Jang, J., Lee, D.S., 2016. Enhanced adsorption of cesium on PVA-alginate encapsulated Prussian blue-graphene oxide hydrogel beads in a fixed-bed column system. Bioresource Technology 218, 294-300.

Kim, Y., Eom, H.H., Kim, Y.K., Harbottle, D., Lee, J.W., 2020. Effective removal of cesium from wastewater via adsorptive filtration with potassium copper hexacyanoferrate-immobilized and polyethyleneimine-grafted graphene oxide. Chemosphere 250, 126262.

Kim, Y., Kim, Y.K., Kim, S., Harbottle, D., Lee, J.W., 2017a. Nanostructured potassium copper hexacyanoferrate-cellulose hydrogel for selective and rapid cesium adsorption. Chemical Engineering Journal 313, 1042-1050.

Kim, Y.K., Kim, T., Kim, Y., Harbottle, D., Lee, J.W., 2017b. Highly effective Cs(+) removal by turbidity-free potassium copper hexacyanoferrate-immobilized magnetic hydrogels. J Hazard Mater 340, 130-139.

Kim, Y.K., Kim, Y., Kim, S., Harbottle, D., Lee, J.W., 2017c. Solvent-assisted synthesis of potassium copper hexacyanoferrate embedded 3D-interconnected porous hydrogel for highly selective and rapid cesium ion removal. Journal of Environmental Chemical Engineering 5, 975-986.

Lee, H., Dellatore, S.M., Miller, W.M., Messersmith, P.B., 2007. Mussel-inspired surface chemistry for multifunctional coatings. Science 318, 426-430.

Lee, W., Lee, J.U., Jung, B.M., Byun, J.-H., Yi, J.-W., Lee, S.-B., Kim, B.-S., 2013. Simultaneous enhancement of mechanical, electrical and thermal properties of graphene oxide paper by embedding dopamine. Carbon 65, 296-304.

Liu, Y.L., Ai, K.L., Lu, L.H., 2014. Polydopamine and Its Derivative Materials: Synthesis and Promising Applications in Energy, Environmental, and Biomedical Fields. Chem Rev 114, 5057-5115.

Long, H., Wu, P., Zhu, N., 2013. Evaluation of Cs+ removal from aqueous solution by adsorption on ethylamine-modified montmorillonite. Chemical Engineering Journal 225, 237-244.

Ma, B., Oh, S., Shin, W.S., Choi, S.-J., 2011. Removal of Co2+, Sr2+ and Cs+ from aqueous solution by phosphate-modified montmorillonite (PMM). Desalination 276, 336-346.

Mobtaker, H.G., Yousefi, T., Pakzad, S.M., 2016. Cesium removal from nuclear waste using a magnetical CuHCNPAN nano composite. J Nucl Mater 482, 306-312.

Niu, H.Y., Wang, S.H., Zeng, T., Wang, Y.X., Zhang, X.L., Meng, Z.F., Cai, Y.Q., 2012. Preparation and characterization of layer-by-layer assembly of thiols/Ag nanoparticles/polydopamine on PET bottles for the enrichment of organic pollutants from water samples. J Mater Chem 22, 15644-15653.

Park, Y., Lee, Y.C., Shin, W.S., Choi, S.J., 2010. Removal of cobalt, strontium and cesium from radioactive laundry wastewater by ammonium molybdophosphate-polyacrylonitrile (AMP-PAN). Chem Eng J 162, 685-695.

Prajitno, M.Y., Harbottle, D., Hondow, N., Zhang, H., Hunter, T.N., 2020. The effect of pre-activation and milling on improving natural clinoptilolite for ion exchange of cesium and strontium. Journal of Environmental Chemical Engineering 8.

Pushkarev, V.V., Skrylev, L.D., Bagretsov, V.F., 1960. EXTRACTION OF RADIOACTIVE CESIUM BY MIXED HEAVY METAL FERROCYANIDES. Zhur.priklad.khim 33.

Qu, H., Caruntu, D., Liu, H., O'Connor, C.J., 2011. Water-Dispersible Iron Oxide Magnetic Nanoparticles with Versatile Surface Functionalities. Langmuir 27, 2271-2278.

Roh, H., Kim, Y., Kim, Y.K., Harbottle, D., Lee, J.W., 2019. Amino-functionalized magnetic chitosan beads to enhance immobilization of potassium copper hexacyanoferrate for selective Cs+ removal and facile recovery. RSC Advances 9, 1106-1114.

Sangvanich, T., Sukwarotwat, V., Wiacek, R.J., Grudzien, R.M., Fryxell, G.E., Addleman, R.S., Timchalk, C., Yantasee, W., 2010. Selective capture of cesium and thallium from natural waters and simulated wastes with copper ferrocyanide functionalized mesoporous silica. Journal of Hazardous Materials 182, 225-231.

Tawil, N., Sacher, E., Boulais, E., Mandeville, R., Meunier, M., 2013. X-ray Photoelectron Spectroscopic and Transmission Electron Microscopic Characterizations of Bacteriophage–Nanoparticle Complexes for Pathogen Detection. The Journal of Physical Chemistry C 117, 20656-20665.

Turgis, R., Arrachart, G., Delchet, C., Rey, C., Barré, Y., Pellet-Rostaing, S., Guari, Y., Larionova, J., Grandjean, A., 2013. An Original “Click and Bind” Approach for Immobilizing Copper Hexacyanoferrate Nanoparticles on Mesoporous Silica. Chemistry of Materials 25, 4447-4453.

Vincent, C., Barré, Y., Vincent, T., Taulemesse, J.M., Robitzer, M., Guibal, E., 2015. Chitin-Prussian blue sponges for Cs(I) recovery: From synthesis to application in the treatment of accidental dumping of metal-bearing solutions. Journal of Hazardous Materials 287, 171-179.

Vincent, T., Vincent, C., Barré, Y., Guari, Y., Le Saout, G., Guibal, E., 2014. Immobilization of metal hexacyanoferrates in chitin beads for cesium sorption: synthesis and characterization. Journal of Materials Chemistry A 2.

Wang, T.-H., Hsieh, C.-J., Lin, S.-M., Wu, D.-C., Li, M.-H., Teng, S.-P., 2010. Effect of Alkyl Properties and Head Groups of Cationic Surfactants on Retention of Cesium by Organoclays. Environmental Science & Technology 44, 5142-5147.

Wei, X., Zhou, Y., Li, Y., Shen, W., 2015. Polymorphous transformation of rod-shaped iron oxides and their catalytic properties in selective reduction of NO by NH3. RSC Advances 5, 66141-66146.

Xu, L.S., Meng, J.X., Yang, P.H., Xu, H.Z., Zhang, S.C., 2021. Cesium-doped layered Li1.2Mn0.54Ni0.13Co0.13O2 cathodes with enhanced electrochemical performance. Solid State Ionics 361.

Yang, H.-M., Jang, S.-C., Hong, S.B., Lee, K.-W., Roh, C., Huh, Y.S., Seo, B.-K., 2016. Prussian blue-functionalized magnetic nanoclusters for the removal of radioactive cesium from water. Journal of Alloys and Compounds 657, 387-393.

Yang, H., Li, H., Zhai, J., Sun, L., Zhao, Y., Yu, H., 2014a. Magnetic prussian blue/graphene oxide nanocomposites caged in calcium alginate microbeads for elimination of cesium ions from water and soil. Chemical Engineering Journal 246, 10-19.

Yang, H., Sun, L., Zhai, J., Li, H., Zhao, Y., Yu, H., 2014b. In situ controllable synthesis of magnetic Prussian blue/graphene oxide nanocomposites for removal of radioactive cesium in water. J. Mater. Chem. A 2, 326-332.

Yang, L., Phua, S.L., Teo, J.K.H., Toh, C.L., Lau, S.K., Ma, J., Lu, X., 2011. A Biomimetic Approach to Enhancing Interfacial Interactions: Polydopamine-Coated Clay as Reinforcement for Epoxy Resin. ACS Applied Materials & Interfaces 3, 3026-3032.

Yu, H.-R., Hu, J.-Q., Liu, Z., Ju, X.-J., Xie, R., Wang, W., Chu, L.-Y., 2017. Ion-recognizable hydrogels for efficient removal of cesium ions from aqueous environment. Journal of Hazardous Materials 323, 632-640.

Yuan, P., Fan, M., Yang, D., He, H., Liu, D., Yuan, A., Zhu, J., Chen, T., 2009. Montmorillonite-supported magnetite nanoparticles for the removal of hexavalent chromium [Cr(VI)] from aqueous solutions. J Hazard Mater 166, 821-829.

Yun Kon Kim, K.B., Yonghwan Kim, David Harbottle, Jae W. Lee, 2018. Immobilization of potassium copper hexacyanoferrate in doubly crosslinked magnetic polymer bead for highly effective Cs+ removal and facile recovery. Journal of Industrial and Engineering Chemistry.

Zhang, H., Hodges, C.S., Mishra, P.K., Yoon, J.Y., Hunter, T.N., Lee, J.W., Harbottle, D., 2020. Bio-Inspired Preparation of Clay-Hexacyanoferrate Composite Hydrogels as Super Adsorbents for Cs(). ACS Appl Mater Interfaces.

Zhang, H., Kim, Y.K., Hunter, T.N., Brown, A.P., Lee, J.W., Harbottle, D., 2017. Organically modified clay with potassium copper hexacyanoferrate for enhanced Cs+ adsorption capacity and selective recovery by flotation. Journal of Materials Chemistry A 5, 15130-15143.